

# Optical coherence microscopy for deep tissue imaging of the cerebral cortex with intrinsic contrast

Vivek J. Srinivasan,<sup>1,\*</sup> Harsha Radhakrishnan,<sup>2</sup> James Y. Jiang,<sup>3</sup> Scott Barry,<sup>3</sup> and Alex E. Cable<sup>3</sup>

<sup>1</sup>MGH/MIT/HMS Athinoula A. Martinos Center for Biomedical Imaging, Department of Radiology, Massachusetts General Hospital/Harvard Medical School, Charlestown, Massachusetts, 02129, USA

<sup>2</sup>Center for Neural Engineering, Pennsylvania State University, University Park, Pennsylvania 16802, USA

<sup>3</sup>Advanced Imaging Group, Thorlabs, Inc., Newton, New Jersey 07860, USA

\*vjsriniv@nmr.mgh.harvard.edu

**Abstract:** *In vivo* optical microscopic imaging techniques have recently emerged as important tools for the study of neurobiological development and pathophysiology. In particular, two-photon microscopy has proved to be a robust and highly flexible method for *in vivo* imaging in highly scattering tissue. However, two-photon imaging typically requires extrinsic dyes or contrast agents, and imaging depths are limited to a few hundred microns. Here we demonstrate Optical Coherence Microscopy (OCM) for *in vivo* imaging of neuronal cell bodies and cortical myelination up to depths of ~1.3 mm in the rat neocortex. Imaging does not require the administration of exogenous dyes or contrast agents, and is achieved through intrinsic scattering contrast and image processing alone. Furthermore, using OCM we demonstrate *in vivo*, quantitative measurements of optical properties (index of refraction and attenuation coefficient) in the cortex, and correlate these properties with laminar cellular architecture determined from the images. Lastly, we show that OCM enables direct visualization of cellular changes during cell depolarization and may therefore provide novel optical markers of cell viability.

©2012 Optical Society of America

**OCIS codes:** (110.4500) Optical coherence tomography; (170.3880) Medical and biological imaging; (170.5380) Physiology; (170.1470) Blood or tissue constituent monitoring; (170.0180) Microscopy; (170.6900) Three-dimensional microscopy.

---

## References and links

1. B. A. Wilt, L. D. Burns, E. T. Wei Ho, K. K. Ghosh, E. A. Mukamel, and M. J. Schnitzer, "Advances in light microscopy for neuroscience," *Annu. Rev. Neurosci.* **32**(1), 435–506 (2009).
2. W. Denk, J. H. Strickler, and W. W. Webb, "Two-photon laser scanning fluorescence microscopy," *Science* **248**(4951), 73–76 (1990).
3. W. Denk and K. Svoboda, "Photon upmanship: why multiphoton imaging is more than a gimmick," *Neuron* **18**(3), 351–357 (1997).
4. E. Beaurepaire, M. Oheim, and J. Mertz, "Ultra-deep two-photon fluorescence excitation in turbid media," *Opt. Commun.* **188**(1–4), 25–29 (2001).
5. P. Theer, M. T. Hasan, and W. Denk, "Two-photon imaging to a depth of 1000  $\mu\text{m}$  in living brains by use of a Ti:Al<sub>2</sub>O<sub>3</sub> regenerative amplifier," *Opt. Lett.* **28**(12), 1022–1024 (2003).
6. D. Kobat, M. E. Durst, N. Nishimura, A. W. Wong, C. B. Schaffer, and C. Xu, "Deep tissue multiphoton microscopy using longer wavelength excitation," *Opt. Express* **17**(16), 13354–13364 (2009).
7. M. Oheim, E. Beaurepaire, E. Chaigneau, J. Mertz, and S. Charpak, "Two-photon microscopy in brain tissue: parameters influencing the imaging depth," *J. Neurosci. Methods* **111**(1), 29–37 (2001).
8. J. A. Izatt, M. R. Hee, G. M. Owen, E. A. Swanson, and J. G. Fujimoto, "Optical coherence microscopy in scattering media," *Opt. Lett.* **19**(8), 590–592 (1994).
9. A. Nimmerjahn, F. Kirchhoff, J. N. Kerr, and F. Helmchen, "Sulforhodamine 101 as a specific marker of astroglia in the neocortex in vivo," *Nat. Methods* **1**(1), 31–37 (2004).

10. J. Binding, J. Ben Arous, J. F. Léger, S. Gigan, C. Boccara, and L. Bourdieu, "Brain refractive index measured in vivo with high-NA defocus-corrected full-field OCT and consequences for two-photon microscopy," *Opt. Express* **19**(6), 4833–4847 (2011).
11. M. Wojtkowski, V. J. Srinivasan, T. H. Ko, J. G. Fujimoto, A. Kowalczyk, and J. S. Duker, "Ultra-high-resolution, high-speed, Fourier domain optical coherence tomography and methods for dispersion compensation," *Opt. Express* **12**(11), 2404–2422 (2004).
12. V. J. Srinivasan, S. Sakadzić, I. Gorczynska, S. Ruvinskaya, W. Wu, J. G. Fujimoto, and D. A. Boas, "Quantitative cerebral blood flow with optical coherence tomography," *Opt. Express* **18**(3), 2477–2494 (2010).
13. G. J. Tearney, M. E. Brezinski, J. F. Southern, B. E. Bouma, M. R. Hee, and J. G. Fujimoto, "Determination of the refractive index of highly scattering human tissue by optical coherence tomography," *Opt. Lett.* **20**(21), 2258 (1995).
14. K. F. Palmer and D. Williams, "Optical-properties of water in near-infrared," *J. Opt. Soc. Am.* **64**(8), 1107–1110 (1974).
15. D. J. Faber, F. J. van der Meer, M. C. G. Aalders, and T. van Leeuwen, "Quantitative measurement of attenuation coefficients of weakly scattering media using optical coherence tomography," *Opt. Express* **12**(19), 4353–4365 (2004).
16. R. Samatham, S. L. Jacques, and P. Campagnola, "Optical properties of mutant versus wild-type mouse skin measured by reflectance-mode confocal scanning laser microscopy (rCSLM)," *J. Biomed. Opt.* **13**(4), 041309 (2008).
17. V. J. Srinivasan, J. Y. Jiang, M. A. Yaseen, H. Radhakrishnan, W. Wu, S. Barry, A. E. Cable, and D. A. Boas, "Rapid volumetric angiography of cortical microvasculature with optical coherence tomography," *Opt. Lett.* **35**(1), 43–45 (2010).
18. W. Drexler, U. Morgner, F. X. Kärtner, C. Pitris, S. A. Boppart, X. D. Li, E. P. Ippen, and J. G. Fujimoto, "In vivo ultrahigh-resolution optical coherence tomography," *Opt. Lett.* **24**(17), 1221–1223 (1999).
19. T. Goto, R. Hatanaka, T. Ogawa, A. Sumiyoshi, J. Riera, and R. Kawashima, "An evaluation of the conductivity profile in the somatosensory barrel cortex of Wistar rats," *J. Neurophysiol.* **104**(6), 3388–3412 (2010).
20. P. Rubio-Garrido, F. Pérez-de-Manzo, C. Porrero, M. J. Galazo, and F. Clascá, "Thalamic input to distal apical dendrites in neocortical layer 1 is massive and highly convergent," *Cereb. Cortex* **19**(10), 2380–2395 (2009).
21. L. E. Enright, S. Zhang, and T. H. Murphy, "Fine mapping of the spatial relationship between acute ischemia and dendritic structure indicates selective vulnerability of layer V neuron dendritic tufts within single neurons in vivo," *J. Cereb. Blood Flow Metab.* **27**(6), 1185–1200 (2007).
22. T. Takano, G. F. Tian, W. Peng, N. Lou, D. Lovatt, A. J. Hansen, K. A. Kasischke, and M. Nedergaard, "Cortical spreading depression causes and coincides with tissue hypoxia," *Nat. Neurosci.* **10**(6), 754–762 (2007).
23. T. H. Chia and M. J. Levene, "Microprisms for in vivo multilayer cortical imaging," *J. Neurophysiol.* **102**(2), 1310–1314 (2009).
24. R. K. Wang, S. L. Jacques, Z. Ma, S. Hurst, S. R. Hanson, and A. Gruber, "Three dimensional optical angiography," *Opt. Express* **15**(7), 4083–4097 (2007).
25. B. J. Vakoc, R. M. Lanning, J. A. Tyrrell, T. P. Padera, L. A. Bartlett, T. Stylianopoulos, L. L. Munn, G. J. Tearney, D. Fukumura, R. K. Jain, and B. E. Bouma, "Three-dimensional microscopy of the tumor microenvironment in vivo using optical frequency domain imaging," *Nat. Med.* **15**(10), 1219–1223 (2009).
26. K. A. Kasischke, E. M. Lambert, B. Panepento, A. Sun, H. A. Gelbard, R. W. Burgess, T. H. Foster, and M. Nedergaard, "Two-photon NADH imaging exposes boundaries of oxygen diffusion in cortical vascular supply regions," *J. Cereb. Blood Flow Metab.* **31**(1), 68–81 (2011).
27. R. A. Stepanoski, A. LaPorta, F. Raccuia-Behling, G. E. Blonder, R. E. Slusher, and D. Kleinfeld, "Noninvasive detection of changes in membrane potential in cultured neurons by light scattering," *Proc. Natl. Acad. Sci. U.S.A.* **88**(21), 9382–9386 (1991).
28. L. T. Perelman, V. Backman, M. Wallace, G. Zonios, R. Manoharan, A. Nusrat, S. Shields, M. Seiler, C. Lima, T. Hamano, I. Itzkan, J. Van Dam, J. M. Crawford, and M. S. Feld, "Observation of periodic fine structure in reflectance from biological tissue: a new technique for measuring nuclear size distribution," *Phys. Rev. Lett.* **80**(3), 627–630 (1998).
29. W. Choi, C. Fang-Yen, K. Badizadegan, S. Oh, N. Lue, R. R. Dasari, and M. S. Feld, "Tomographic phase microscopy," *Nat. Methods* **4**(9), 717–719 (2007).
30. W. Drexler and J. G. Fujimoto, "State-of-the-art retinal optical coherence tomography," *Prog. Retin. Eye Res.* **27**(1), 45–88 (2008).
31. N. R. Kreisman and J. C. LaManna, "Rapid and slow swelling during hypoxia in the CA1 region of rat hippocampal slices," *J. Neurophysiol.* **82**(1), 320–329 (1999).
32. P. G. Aitken, D. Fayuk, G. G. Somjen, and D. A. Turner, "Use of intrinsic optical signals to monitor physiological changes in brain tissue slices," *Methods* **18**(2), 91–103 (1999).
33. M. Müller and G. G. Somjen, "Intrinsic optical signals in rat hippocampal slices during hypoxia-induced spreading depression-like depolarization," *J. Neurophysiol.* **82**(4), 1818–1831 (1999).
34. L. Tao, D. Masri, S. Hrabětová, and C. Nicholson, "Light scattering in rat neocortical slices differs during spreading depression and ischemia," *Brain Res.* **952**(2), 290–300 (2002).
35. T. M. Polischuk, C. R. Jarvis, and R. D. Andrew, "Intrinsic optical signaling denoting neuronal damage in response to acute excitotoxic insult by domoic acid in the hippocampal slice," *Neurobiol. Dis.* **4**(6), 423–437 (1998).
36. R. D. Andrew, C. R. Jarvis, and A. S. Obeidat, "Potential sources of intrinsic optical signals imaged in live brain slices," *Methods* **18**(2), 185–196, 179 (1999).

37. M. E. Moseley, Y. Cohen, J. Kucharczyk, J. Mintorovitch, H. S. Asgari, M. F. Wendland, J. Tsuruda, and D. Norman, "Diffusion-weighted MR imaging of anisotropic water diffusion in cat central nervous system," *Radiology* **176**(2), 439–445 (1990).
  38. M. E. Moseley, Y. Cohen, J. Mintorovitch, L. Chileuitt, H. Shimizu, J. Kucharczyk, M. F. Wendland, and P. R. Weinstein, "Early detection of regional cerebral-ischemia in cats - comparison of diffusion-weighted and T2-weighted MRI and spectroscopy," *Magn. Reson. Med.* **14**(2), 330–346 (1990).
  39. M. Hoehn-Berlage, D. G. Norris, K. Kohno, G. Mies, D. Leibfritz, and K. A. Hossmann, "Evolution of regional changes in apparent diffusion coefficient during focal ischemia of rat brain: the relationship of quantitative diffusion NMR imaging to reduction in cerebral blood flow and metabolic disturbances," *J. Cereb. Blood Flow Metab.* **15**(6), 1002–1011 (1995).
  40. H. Wang, A. J. Black, J. F. Zhu, T. W. Stigen, M. K. Al-Qaisi, T. I. Netoff, A. Abosch, and T. Akkin, "Reconstructing micrometer-scale fiber pathways in the brain: multi-contrast optical coherence tomography based tractography," *Neuroimage* **58**(4), 984–992 (2011).
  41. P. J. Basser, J. Mattiello, and D. LeBihan, "MR diffusion tensor spectroscopy and imaging," *Biophys. J.* **66**(1), 259–267 (1994).
  42. D. S. Tuch, "Q-ball imaging," *Magn. Reson. Med.* **52**(6), 1358–1372 (2004).
  43. V. J. Wedeen, P. Hagmann, W. Y. I. Tseng, T. G. Reese, and R. M. Weisskoff, "Mapping complex tissue architecture with diffusion spectrum magnetic resonance imaging," *Magn. Reson. Med.* **54**(6), 1377–1386 (2005).
- 

## 1. Introduction

Staining methods used by Golgi, Cajal, and Nissl led to seminal observations about the microscopic organization of the brain. Even today, cyto-architecture in the brain is studied by staining of bulk tissues, specific cell populations, or organelles in histological specimens followed light microscopic observation. More recently, advances in light microscopy [1] and cell-labeling techniques have enabled *in vivo* imaging of neuro-anatomy and function. Two-photon microscopy [2,3], in particular, has become the method of choice for *in vivo* cortical imaging up to depths of a few hundred microns. However, two-photon microscopy typically requires either exogenous dyes or genetic labeling and costly, bulky femtosecond lasers. Imaging depths approaching a millimeter can be achieved with two-photon microscopy using sparse labeling and regenerative amplifiers [4,5] or longer wavelength excitation [6]. Fundamental limits to the penetration depth of two-photon microscopy are set by attenuation from scattering [7], although aberrations and out-of-focus fluorescence may also degrade contrast at larger imaging depths [5].

Here, we introduce an original *in vivo* cellular brain imaging strategy that uses intrinsic contrast, i.e. contrast arising from endogenous tissue properties. Using an Optical Coherence Microscopy (OCM) system and image processing procedures to synthesize images from dynamically focused data sets, we achieve imaging of cortical myelination and neuronal cell bodies at depths of 1.3 mm in the rat cortex. As compared to confocal reflectance microscopy, which possesses similar contrast mechanisms, OCM achieves a higher imaging depth through rejecting multiply scattered and out-of-focus light [8]. We confirm known lamina-specific features in cell density, size and myelination, and perform high-resolution angiography of the capillary network. We also use this novel imaging platform to measure the average refractive index and scattering properties of brain tissue, and directly relate these bulk optical properties to laminar variations in tissue cellular architecture. Finally, we demonstrate changes in cellular morphology and contrast during both transient and permanent cell depolarization.

## 2. Experimental methods

### 2.1 Animal preparation

For structural OCM measurements, Sprague Dawley rats (220-320 g) were temperature controlled, anesthetized with isoflurane (1.5-2% in a mixture of O<sub>2</sub> and air) and tracheotomized. A catheter was inserted into the femoral artery for measuring blood gases and monitoring blood pressure. Another catheter was inserted into the femoral vein for administering anesthesia and paralytics, where applicable. A sealed cranial window was created in the center of the parietal bone with the dura removed. For some experiments, SR101 was dissolved in ACSF and applied directly to the cortical surface for 3-5 minutes, and rinsed with saline at 37 degrees, as previously described [9]. Isoflurane was discontinued and

anesthesia maintained with a 50 mg/kg intravenous bolus of alpha-chloralose followed by continuous intravenous infusion at 40 mg/(kg h). During the imaging, rats were ventilated with a mixture of air and O<sub>2</sub>. Imaging was performed through the sealed cranial window. The systemic arterial blood pressure was 95-110 mmHg, pCO<sub>2</sub> was 35-44 mmHg, and pO<sub>2</sub> was 95-110 mmHg. Cortical spreading depression was induced by application of 1 M KCl to the cortical surface through a burr hole located 2 mm away from the imaging field. We administered an intravenous bolus of pancuronium bromide (2 mg kg<sup>-1</sup>) followed by continuous intravenous infusion at 2 mg kg<sup>-1</sup> h<sup>-1</sup> during the cortical spreading depression experiments to minimize possible animal motion. Anoxic depolarization was induced by intravenous injection of a bolus of 1 M KCl. All experimental procedures were approved by the Massachusetts General Hospital Sub-committee on Research Animal Care.

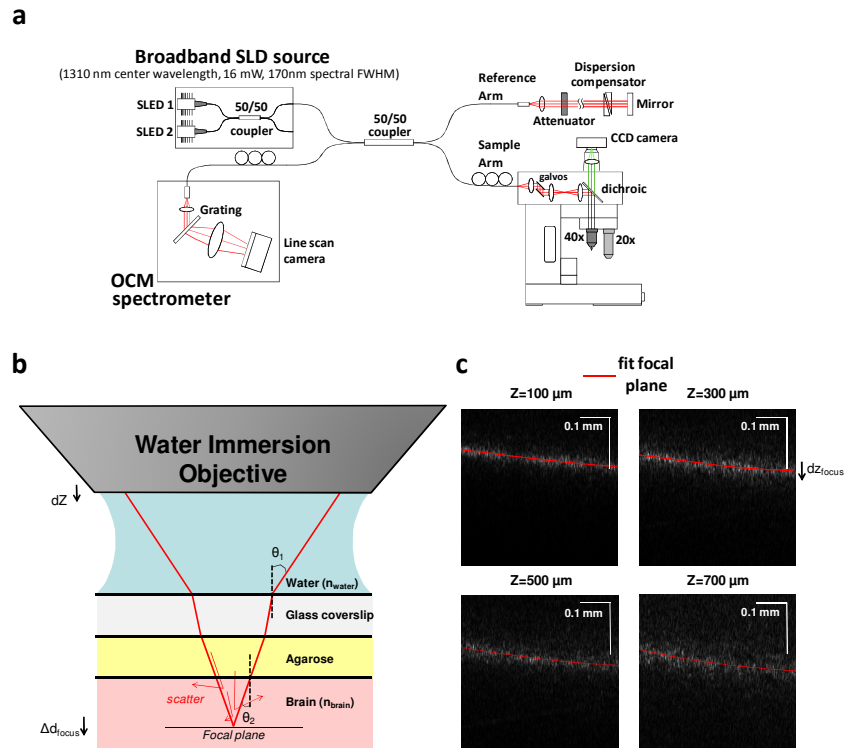


Fig. 1. Optical Coherence Microscopy (OCM) system for deep tissue brain imaging. (a) OCM system schematic. (b) Zoom of ray optics diagram. (c) Two dimensional cross-sectional images with focus fit. By successive application of Snell's law at each interface, it is possible to determine the derivative of the path length to the focus ( $Z_{\text{focus}}$ ) with respect to the objective assembly translation ( $Z$ ), in terms of the local brain refractive index, as described in the Experimental methods.

## 2.2 Imaging and data acquisition

The experimental system used in our studies is shown in Fig. 1. A 1310 nm spectral/Fourier domain OCM microscope, shown in Fig. 1(a), was constructed for *in vivo* imaging of the rat cerebral cortex. The light source consisted of two unpolarized superluminescent diodes combined using a 50 / 50 fiber coupler to yield a bandwidth of 170 nm. The axial (depth) resolution was 4.7  $\mu\text{m}$  in air (3.5  $\mu\text{m}$  in tissue). The power on the sample was 4 mW, and the sensitivity was 105 dB. A spectrometer with a 1024 pixel InGaAs line scan camera operated at 47,000 axial scans per second. For OCM angiography, a 20x water immersion objective (Olympus XLUMPLFL20XW/IR-SP, 20X, NA 0.95) achieved a transverse resolution of 1.8

microns (full-width at half-maximum of the intensity profile). For OCM structural imaging, a 40x water immersion objective (Olympus LUMPLANFL/IR 40X W, NA 0.8) achieved a transverse resolution of 0.9 microns (full-width at half-maximum of the intensity profile), corresponding to a depth of focus of approximately 3.8 microns. Notably, for structural imaging, the depth of focus (3.8 microns) was comparable to the axial resolution (3.5 microns). This represents a departure from conventional OCM, where the depth of focus is larger than the axial resolution. The imaging field-of-view was approximately 620 microns. Distilled water was used for the immersion medium. The imaging geometry is shown in Fig. 1(b). The light passes successively through water, the glass coverslip, agarose placed on the brain, and finally, the brain itself. At each interface, it is possible to apply Snell's law to determine refraction of rays. The whole microscopic assembly is translated up or down relative to the brain to change the focus position. At the same time, OCM enables accurate determination of the change in the path length to the focus. The optical path length to the focal plane is decreased due to a reduction in the height of the water meniscus, and increased due to the focal plane moving further into the brain. By measuring the change in the path length to the focal plane from OCM image analysis, it is possible to solve for the local refractive index in the brain [10].

The sample arm assembly was initially set so that the optical focus was just above the cortical surface, and translated in increments of 5 microns for the 40x objective, and 10 microns for the 20x objective. At each focusing depth a three-dimensional data set was acquired. Thus, a four-dimensional data set was generated, with dimensions corresponding to x position, y position, path length (z), and the sample arm assembly translation of Z. Here we use Z to denote a physical translation of the sample arm assembly, and z to denote the path length (group delay). The raw OCM data could thus be described as  $A(x,y,z,Z)$ , where A is the OCM signal amplitude at a particular (x,y,z) position, corresponding to a particular sample arm assembly translation of Z. A fitting procedure (described below) was used to determine the path length to the focus as a function of x,y, and Z, i.e.  $z_{\text{focus}}(x,y,Z)$ .

Data from the InGaAs camera (Sensors Unlimited) was acquired using a Coreco X64-CL Express frame grabber on a Dell Precision T3400 computer (2.66 GHz, 3.25 GB RAM). A real-time cross-sectional display enabled positioning of the optical focus relative to the brain surface. Data corresponding to a three-dimensional volume was acquired at each focus position. Each volume was stored in a file consisting of 512 frames (y pixels) with 512 axial scans (x pixels) per frame. The raw spectral data was stored for each x,y position, and the axial scan was reconstructed in post-processing in Matlab 7.4 (Natick, MA) using methods previously described [11,12]. Each spectrum consisted of 1024 pixels with two bytes per pixel. Therefore, each three-dimensional volume at each depth consisted of 536,870,912 bytes. The required data storage could be significantly reduced since the axial (depth) range required for each data set (typically  $\sim < 100$  microns) is significantly smaller than the total depth range (1.5 mm) due to the high numerical aperture.

### 2.3 Data processing

It is possible to relate a particular path delay in the OCM image (z) with a depth in the brain ( $d_{\text{brain}}$ ) through the following equation:

$$z(d_{\text{brain}}, Z) = z_0 + \int_{z=0}^{d_{\text{brain}}} f n_{\text{brain}}(z) dz - f n_{\text{water}} Z \quad (1)$$

where  $z_0$  represents a path length delay offset. (For convenience, we have neglected the positive and negative path delay degeneracy inherent to spectral / Fourier domain OCM systems.) The group refractive index is assumed to equal a constant fraction f of the phase refractive index for both the brain and water. The above expression can be used to relate a particular single-pass path delay (z) in the OCM image to a particular physical depth in the brain  $d_{\text{brain}}$ , provided that the refractive index profile as a function of depth in the brain is known up to this particular depth. Thus a particular translation of the focusing assembly and a

particular depth ( $d_{\text{brain}}$ ) in the brain will uniquely determine a path length. By taking the differential of the above expression, we obtain,

$$dz = f n_{\text{brain}} \Delta d_{\text{brain}} - f n_{\text{water}} dZ \quad (2)$$

In particular, by centering our attention on the location of the focus, the following expression is obtained:

$$dz_{\text{focus}} = f n_{\text{brain}} \Delta d_{\text{focus}} - f n_{\text{water}} dZ \quad (3)$$

By repeated application of Snell's law at each interface, and assuming a small-angle approximation ( $\sin(\theta) = \theta$ , valid even for marginal rays at  $\theta \approx 23^\circ$ ), it can be shown that the shift of the focus when the focusing assembly is translated is given by [13]:

$$\Delta d_{\text{focus}} = dZ \frac{n_{\text{brain}}}{n_{\text{water}}} \quad (4)$$

Finally, by substitution we obtain an expression which relates the refractive index to the focus translation.

$$dz_{\text{focus}} = f \left( dZ \frac{n_{\text{brain}}^2 - n_{\text{water}}^2}{n_{\text{water}}} \right) \quad (5)$$

For all calculations,  $n_{\text{water}}$  was assumed to be 1.324 and  $f$  was assumed to be 1.02 [14]. Therefore, by measuring the change in the path length to the focal plane as the sample arm assembly is translated, it is possible to solve for the local refractive index of the brain at the focal plane. At each depth, a curve was fit to the focal plane, as shown in Fig. 1(c). Thus we were able to determine the derivative of  $z_{\text{focus}}$  with respect to  $Z$ . From this data we were able to determine the brain refractive index as a function of  $d_{\text{brain}}$ .

We used a single scattering model to describe the OCM signal as a function of path length difference ( $z$ ), as shown below [15]

$$A(x, y, z, Z) \sim \frac{B[d_{\text{brain}}(x, y, z, Z)]}{\sqrt{\left(\frac{z - z_{\text{focus}}(x, y, Z)}{z_R}\right)^2 + 1}} \exp\left[-2 \int_0^{d_{\text{brain}}(x, y, z, Z)} \mu_t(z') f n_{\text{brain}}(z') dz'\right] \quad (6)$$

We have neglected the effects of water absorption in the above expression. It should also be noted that we corrected our data for the spectrometer response function, which describes the sensitivity roll-off of the spectrometer as a function of path length  $z$ . It is important to realize that the peak of the above function does not necessarily occur at  $z = z_{\text{focus}}$ . In fact, the path delay with the peak intensity in the OCM data will necessarily occur more superficially than  $z_{\text{focus}}$ . Finally we have included a term,  $B(d_{\text{brain}})$ , which accounts for possible differences in backscattering from different layers in the brain.

We noticed a broadening of the reflectance profile (an apparent increase of  $z_R$ ) with increasing focusing depth, most likely due to multiple scattered light that is detected and possibly, spherical aberrations. We anticipate that this broadening effect could be used in the future to estimate the scattering anisotropy, as it results from multiple scattered light which is detected in the confocal geometry.

If we consider the signal from  $z = z_{\text{focus}}$ , at  $d_{\text{focus}}(x, y, Z) = d_{\text{brain}}(x, y, z_{\text{focus}}(Z), Z)$ , we obtain

$$A(x, y, z_{\text{focus}}(Z), Z) \sim \sqrt{B[d_{\text{focus}}(x, y, Z)]} \exp\left[- \int_0^{d_{\text{focus}}(x, y, Z)} \mu_t(z') f n_{\text{brain}}(z') dz'\right] \quad (7)$$

Thus, the signal from the focus is indicative of the double pass attenuation experienced up to the focal plane, and the backscattering from the focal plane. The backscattering from the focal plane, in turn, depends on the backscattering cross-section of the tissue constituents in the focal plane. It is convenient to take the logarithm of the OCM signal from the focus as shown below:

$$\log[A(x,y,z_{\text{focus}}(Z),Z)] \sim \log\left[\sqrt{B[d_{\text{focus}}(x,y,Z)]}\right] - \int_0^{d_{\text{focus}}(x,y,Z)} \mu_t(z) f_{\text{brain}}(z) dz' \quad (8)$$

By taking the derivative of the above expression with respect to  $Z$ , and assuming that both  $\mu_t(d_{\text{brain}})$  and  $n_{\text{brain}}(d_{\text{brain}})$  are piecewise constant, we obtain:

$$\frac{d}{dZ} \left\{ \log[A(x,y,z_{\text{focus}}(Z),Z)] \right\} \sim \frac{d}{dZ} \left\{ \log\left[\sqrt{B[d_{\text{focus}}(x,y,Z)]}\right] \right\} - \mu_t[d_{\text{focus}}(x,y,Z)] f \frac{\left\{ n_{\text{brain}}[d_{\text{focus}}(x,y,Z)] \right\}^2}{n_{\text{water}}} \quad (9)$$

It is expedient to neglect changes the backscattering term (the first term on the right-hand side) in the above equation for homogenous layers, where the cellular constituents do not change appreciably. Given this assumption, by plotting the logarithm of the OCM signal from the focus as a function of  $d_{\text{focus}}$ , and performing piecewise linear fitting, it should be possible to determine the local attenuation coefficient (the second term on the right-hand side in the above equation).

In reality, due to the detection of multiple scattering, the attenuation coefficient does not accurately reflect the scattering coefficient,  $\mu_s$ . Rather, the attenuation coefficient is given by the scattering coefficient times an anisotropy ( $g$ ) dependent factor  $a(g)$  that decreases as  $g$  increases [16].

$$\mu_t = a(g)\mu_s \quad (10)$$

Therefore, an increase in  $\mu_t$  may be accounted for by *either* an increase in  $\mu_s$  or a decrease in  $g$  (and hence an increase in  $a(g)$ ). However, due to our high numerical aperture and the fact that the signal was only examined at path lengths corresponding to the focus, we achieved improved rejection of multiple scattered light. The differences in  $\mu_t$  between cortical layers are therefore attributable predominantly to differences in  $\mu_s$ , but we cannot rule out the contribution of differences in  $g$  to the measured attenuation coefficient. In particular, we expect that the anisotropy ( $g$ ) of gray matter should be higher than that of white matter, which may partially account for the observed differences in  $\mu_t$  observed below.

#### 2.4 Image processing

For image viewing, the four-dimensional data set was averaged to form a three-dimensional data set, designed to depict the reflectivity at each location in the brain. This averaging step was essential for speckle reduction. In principle, each position in the brain can be related to a particular voxel for each acquired 3D OCM data set. The final, weighted average could be constructed as follows:

$$\hat{A}(x, y, d_{\text{brain}}) = \sum_i w[z(d_{\text{brain}}, Z_i) - z_{\text{focus}}(x, y, Z_i)] A[x, y, z(d_{\text{brain}}, Z_i), Z_i] \quad (11)$$

Subpixel shifts were accounted for by upsampling. The choice of the weighting function represents a tradeoff between speckle reduction and resolution loss. One possibility for the weighting function is  $w(z - z_{\text{focus}}) = \delta(z - z_{\text{focus}})$ , which would only include only information obtained precisely from the path length corresponding focal plane. However, we found that the inclusion of information obtained from path lengths away from the focal plane was essential for high quality images. Thus, for a slight loss in resolution we were able to obtain a significantly less speckled image.

Another issue for discussion is the detection of the focal plane  $z_{\text{focus}}$ . A number of metrics are possible, including either maximizing the intensity or maximizing the image sharpness. We found that the depth of maximum intensity did not always correspond to the depth of maximum sharpness. In particular, the depth of maximum sharpness shifted to larger path lengths relative to the depth of maximum intensity as the focus was translated deeper in scattering tissue. Therefore, we used a sharpness metric to determine the path length to the

focus. We expect that further improvements could be achieved by accounting for the contribution of multiply scattered light in the weighting function.

### *Neurons*

Cell bodies manifested themselves as low scattering regions against a highly scattering “background” of neurites. In particular, appropriate normalization of intensity was essential in order to consistently and clearly visualize neuronal cell bodies. Blood vessels created shadows in the OCM data that caused uniform decreases in intensity. Therefore, normalization of each pixel relative to its surroundings was performed, prior to taking a minimum intensity projection to visualize the OCM data. Normalization was also performed to account for variations in intensity caused by confocal gating. Images were displayed in grayscale.

### *Myelin*

Myelinated axons manifested themselves as highly backscattering regions. In particular, the high refractive index of the lipid rich myelin sheath leads to highly directional backscattering. To visualize myelinated axons, normalization of each pixel relative to its surroundings was performed, prior to taking a maximum intensity projection to visualize the OCM data. Images were displayed in inverted grayscale. Where a depth range is displayed on the image, a maximum intensity projection was also performed over multiple focal positions to improve continuity of myelin processes.

### *Angiography*

In order to reduce sensitivity to motion artifacts, a transverse resolution of 1.8 microns (full-width at half-maximum of the intensity profile) was used. Data were acquired by translating the objective in steps of 10 microns, and acquiring an OCM angiogram at each depth, as previously described [17]. The OCM angiography scan protocol consisted of 1024 frames (512 y locations and 2 frames per y location) and 512 axial scans per frame. After axial motion correction, the absolute value of the difference in the complex OCT amplitude images obtained from the same y location was computed [17]. Thus, a four-dimensional data set was generated, with dimensions corresponding to x position, y position, path length (z), and the sample arm assembly translation (Z). For each translation position (focusing depth), we used Gaussian axial (z) windowing (FWHM = 70 microns, centered about the focus) and image fusion [18] techniques to simultaneously reduce speckle while maintaining high transverse resolution. Thus the four-dimensional angiogram data set could be reduced to a three-dimensional data set. To appropriately weight the angiogram brightness, accounting for these noise sources, we introduced a normalization function,  $(K^2 + A_{\text{lpf}}^2)^{1/2}$ , where  $A_{\text{lpf}}$  is the low-pass filtered (blurred) OCT scattering image, and K is a constant which is chosen to prevent shot noise amplification in low intensity regions. The weighting procedure increases the contribution of deeper layers to the maximum intensity projection.

### *Statistics*

Index of refraction measurements and OCM signal slope measurements were calculated in layer I, layer II/III, layer IV, and layer V in  $n = 17$  animals. Data were expressed as mean  $\pm$  standard error of mean (SEM). Statistical comparisons were done using one-way ANOVA followed by post hoc group comparisons using Tukey's honestly significant differences test ( $\alpha = 0.05$ ).



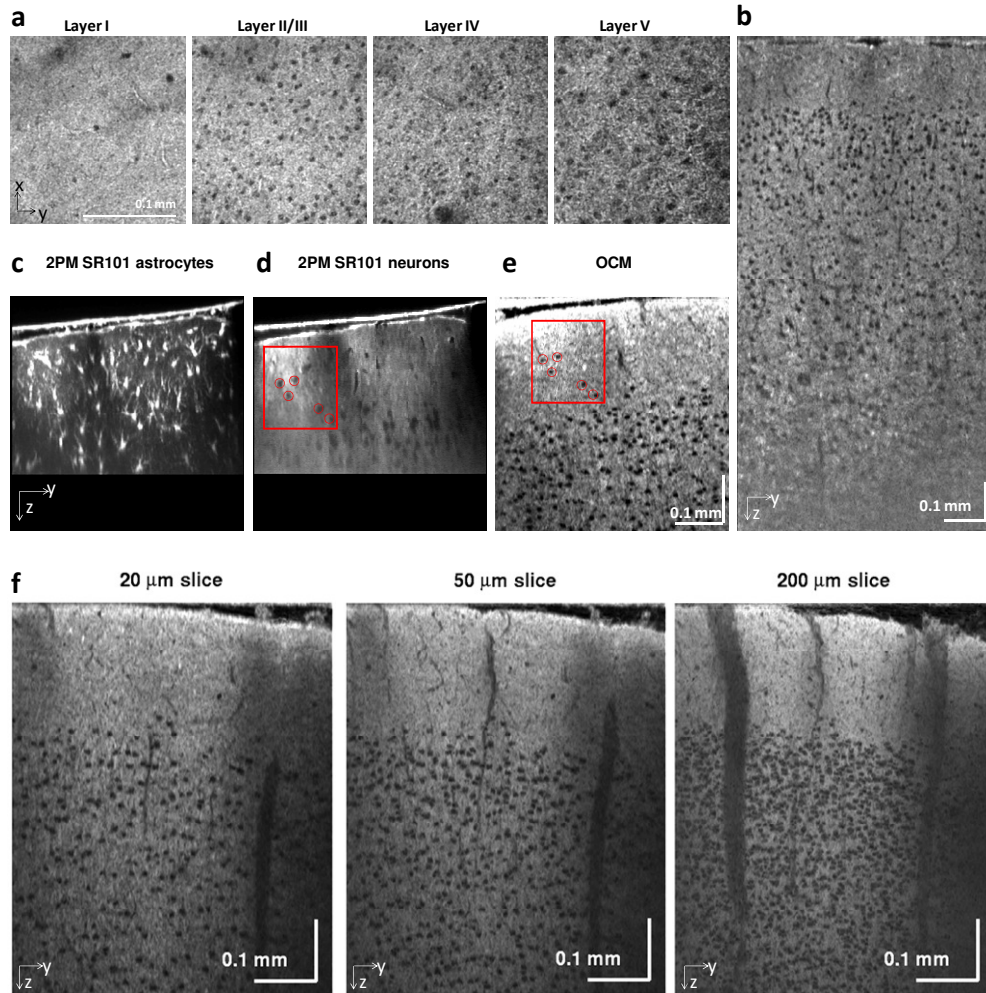


Fig. 2. OCM neuronal imaging. (a) OCM cellular images at different cortical depths, showing expected laminar differences between cortical layers. (b) A virtual coronal section of the rat somatosensory S1 cortex shows clear delineation of layers. This includes a thin layer near the cortical surface with few neurons, as well as supragranular, granular, and infragranular layers. (c) Maximum intensity projection image of a 20 micron coronal slice from two-photon microscopy data with SR101-staining, showing astrocytes as bright regions. (d) Minimum intensity projection image of a 20 micron coronal slice from two-photon microscopy data with SR101-staining, showing neurons as dark quasi-spherical regions. (e) Minimum intensity projection image of OCM data from the same 20 micron coronal slice, showing dark regions that correspond closely with those in (d). A red box is drawn around a region in cortical layer I, and neurons are circled. (f) OCM performs in vivo "histology". A volumetric, dynamically focused data set (5 micron steps), is used to extract coronal sections (slices) of different thicknesses, without actually cutting the tissue.

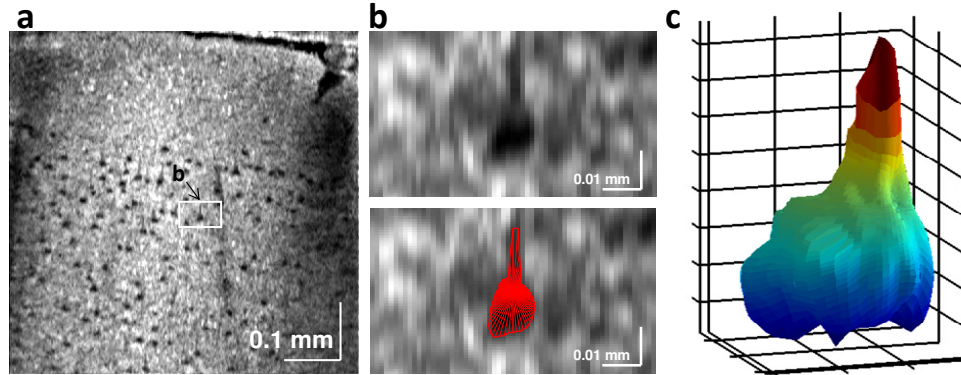


Fig. 3. (a) 8.5 micron minimum intensity projection OCM slice with a white rectangle drawn around a region of interest approximately 300 microns beneath the cortical surface. (b) zoom of raw OCM image around region of interest (above), with red rays drawn from origin of a spherical coordinate system to locations where the interpolated OCM data first exceeds an empirically set threshold (below). (c) Parametric surface plot using a spherical coordinate system, showing a neuron-like morphology, and possible visualization of a portion of the apical dendrite (Media 1).

### 3. Results

Using intrinsic contrast, OCM enables a range of new measurements in the living brain. Here, we investigate the capability of OCM to visualize cell bodies and myelinated axons, perform angiography, quantify tissue scattering properties and refractive index, and determine cell viability through a closed cranial window over the rat neocortex.

#### *OCM visualizes neurons*

Distinct, quasi-spherical regions of low backscattering corresponding to neuronal cell bodies were visualized in our OCM images. The visualization of these “holes” could be enhanced by performing a minimum intensity projection along an axis perpendicular to the viewing plane. The density increased considerably from layer I to layer II/III. The size decreased from layer II/III to layer IV, while increasing noticeably towards layer V (Fig. 2(a)). Figure 2(b) shows a 20 micron coronal slice over a 1.2 mm depth, clearly demonstrating these trends. Contrast typically degraded past 1 mm, although in some animals, imaging depths of up to 1.3 mm depth was possible. Figure 2(c)–2(e) shows a comparison between OCM and sulforhodamine 101 (SR101)-stained two-photon microscopy images of the same 20 micron coronal slice. Neurons are known not to take up SR-101 [9]; therefore, neurons could be visualized as dark regions in a minimum intensity projection of the SR-101 channel data, while astrocytes, which take up SR-101, could be visualized through a maximum intensity projection of the SR-101 channel data. The images show a close correspondence between “holes” in the two-photon microscopy data set and “holes” in the OCM data set. Furthermore, the morphology of some of the “holes” in the OCM data set corresponded to that of pyramidal neurons (Fig. 3 and Media 1).

Taken together, these data suggests that OCM has preferential contrast for neurons. Therefore, OCM may function similarly to Nissl-staining and histology, except that OCM imaging can be performed non-invasively over time, without the need for exogenous dyes or contrast agents. To further illustrate this concept, Fig. 2(f) shows virtual coronal slices of different thicknesses (20, 50, and 200 microns), obtained from the same volumetric OCM data set. These images could, in principle, be repeated longitudinally in the same animal over time.

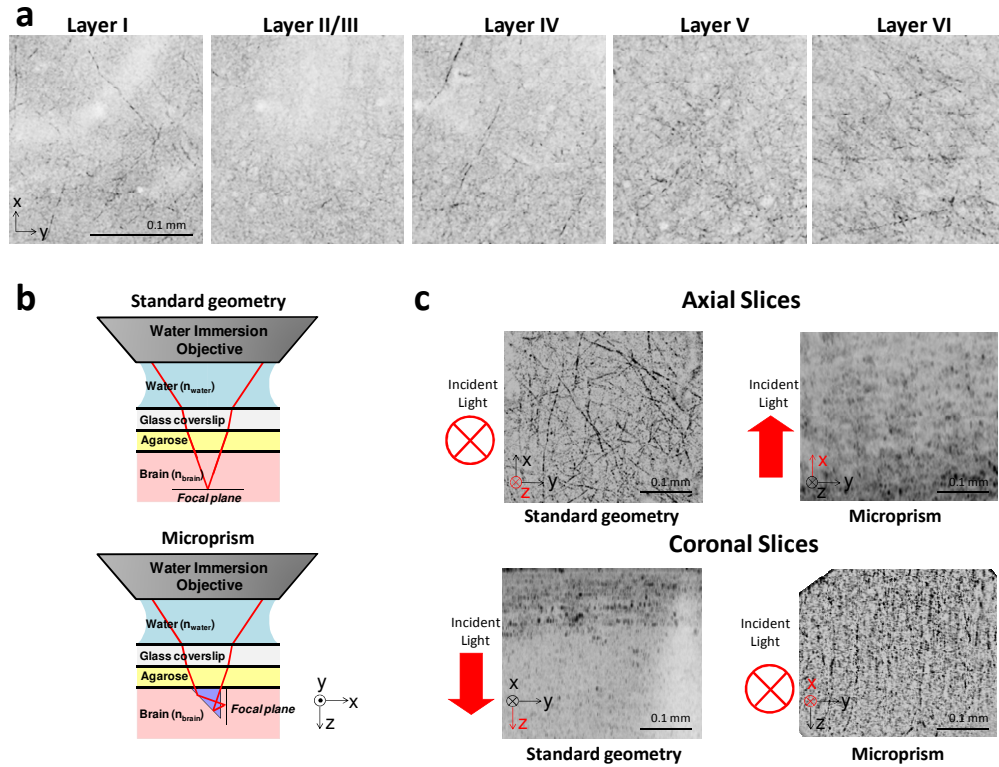


Fig. 4. OCM myelin imaging. (a) Imaging of myelination in different cortical layers shows the expected laminar characteristics, with increased myelination in layer IV and below. In addition, myelinated axons exhibit orientation-dependent backscattering characteristics, so that only orientations perpendicular to the incident light are visualized. To investigate this phenomenon, a microprism was used to rotate the imaging geometry by 90 degrees (b, incident light from the x-direction). In addition, imaging in the conventional geometry was performed (b, incident light from the z-direction). By comparison of axial and coronal slices in the two different imaging geometries, it is evident that the visualization of myelinated axons is highly orientation dependent. In particular, processes with orientations in the *en face* plane (perpendicular to the incident light) are well visualized, whereas others are not (c). The direction of incident light (opposite to the direction of backscattered light) is shown in red.

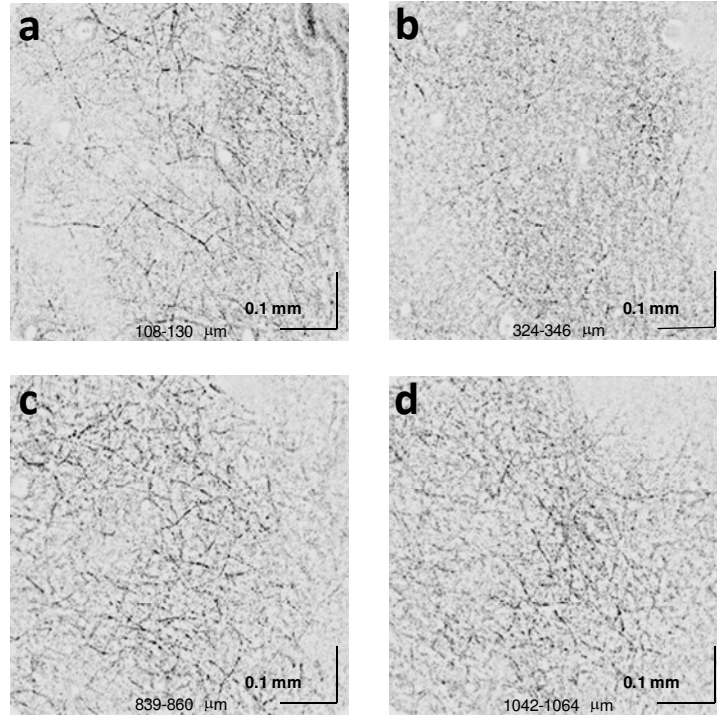


Fig. 5. Laminar distribution of myelination in the rat visual (V1) cortex. Images of myelination at different cortical depths. In particular, a reduction in myelination is seen in layer II-III (b) compared to the other cortical layers.

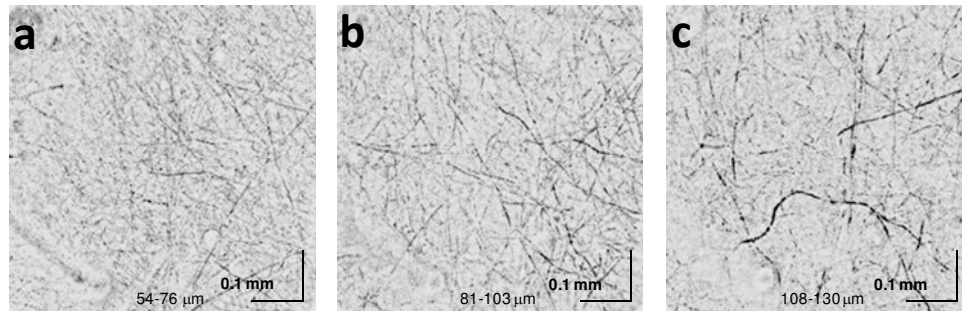


Fig. 6. Laminar distribution of myelination in layer I (Media 2). Thinner myelinated processes are found more superficially (a) while thicker myelinated processes are observed at greater depths (c).



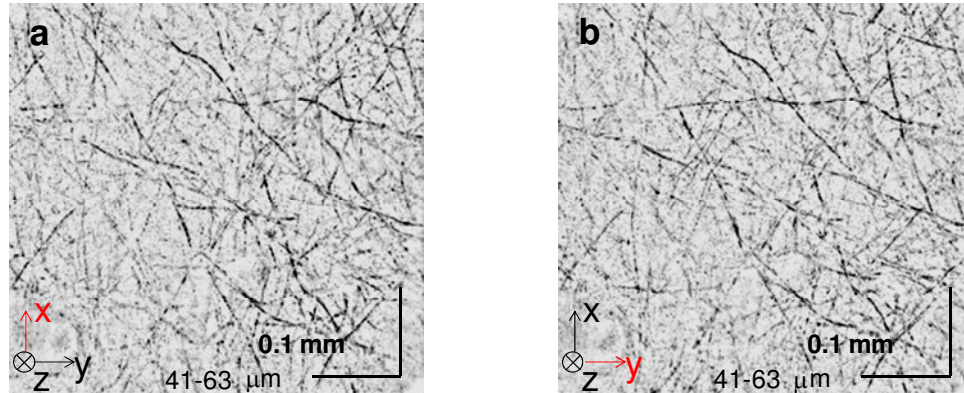


Fig. 7. Backscattering from myelin processes shows no polarization dependence. The contrast with light polarized along the x-axis (a) is virtually identical to the contrast with light polarized along the y-axis (b). The polarization is shown in red, and was achieved by placing a polarizer before the objective lens (Fig. 2(a)).

#### *OCM visualizes cortical myelination*

As shown in Fig. 4, long, highly scattering processes corresponding to myelinated axons were visible in the transverse or *en face* plane. The visualization of myelination could be enhanced through maximum intensity projections along an axis perpendicular to the viewing plane. Myelinated axons in the *en face* plane were prominent in cortical layers I and IV-VI, while being absent in layers II-III, consistent with the known distribution of cortical myelination [19]. This conclusion is also supported by Fig. 5. In particular, the morphology and distribution of horizontal myelinated processes in layer I are very similar to the axons of M-type thalamus cells [20]. Finer processes were seen more superficially, while thicker processes were seen at greater depths (Fig. 6). The contrast of the highly scattering processes in layer I remained during and immediately after anoxic depolarization (data not shown), indicating that the contrast mechanism does not require integrity of axons and dendrites, which undergo beading or blebbing during anoxia [21,22]. Additional investigation revealed little or no polarization dependence in scattering from myelinated axons (Fig. 7). Furthermore, in contrast to fluorescence, which is uniformly generated in all directions, scattering properties of tissue are highly anisotropic. Therefore, OCM contrast is expected to depend critically on the excitation and detection geometries. Rotation of the imaging geometry by 90 degrees using a microprism [23] revealed myelin orientations perpendicular to the cortical surface in layer II/III which were invisible in the standard imaging geometry (Fig. 4(b) and 4(c)). Precise microprism insertion and orientation was required in order to visualize these processes. Myelinated axons can be visualized with OCM due to high refractive index of the lipid-rich myelin sheath. Hence the large backscattering cross-section will be observed only if the myelin sheath is oriented in the plane perpendicular to the optical axis, also known as the *en face* plane. A volumetric rendering of myelination in cortical layer I in the standard imaging geometry is shown (Media 2), displaying a range of transverse orientations.

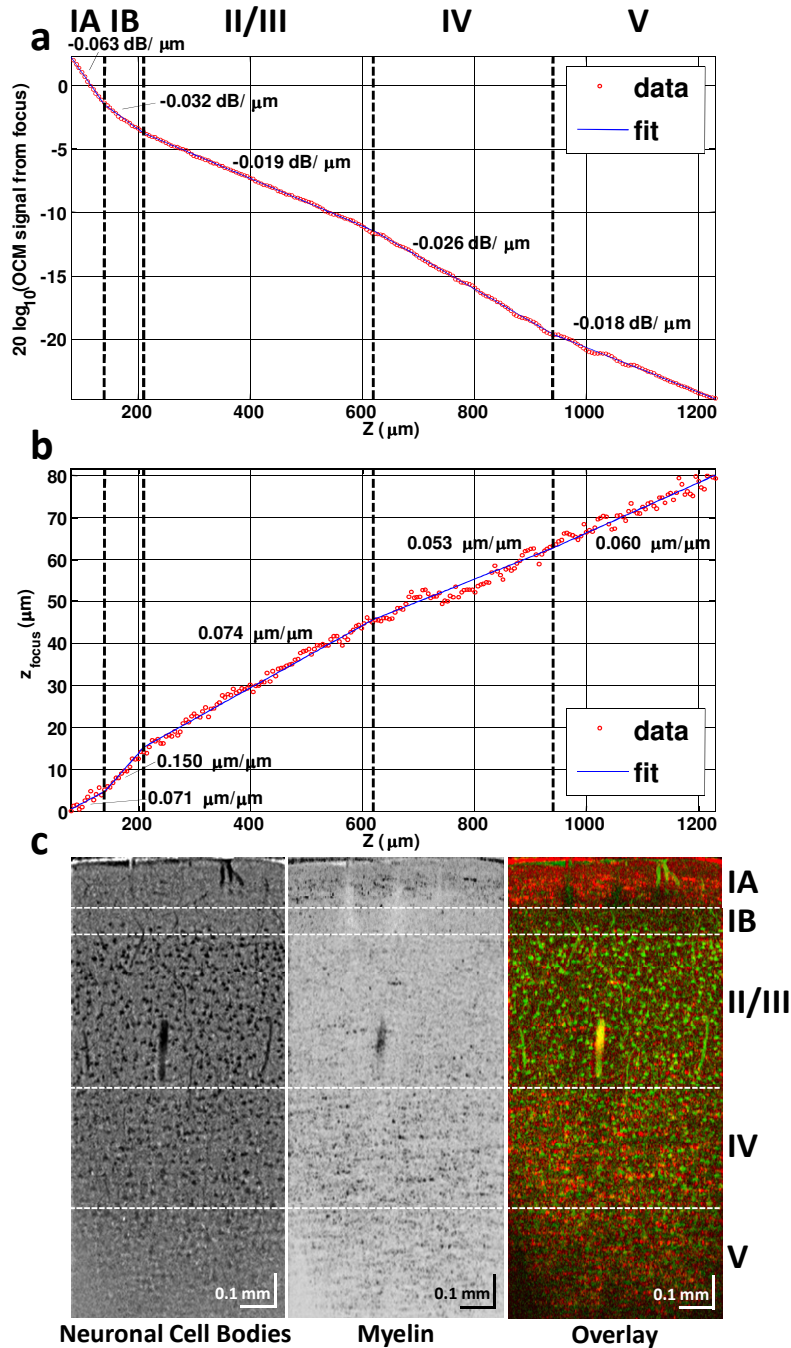


Fig. 8. OCM quantification of optical properties. (a) A piecewise linear fit of the OCM signal from the focus automatically detected 5 regions with different attenuation coefficients, demarcated by dashed lines. (b) Index of refraction measurements were also performed in these 5 regions, based on  $dz_{\text{focus}}/dZ$  (see Experimental methods). (c) The 5 regions with different attenuation coefficients corresponded well to layers IA, IB, II/III, IV, and V. In order to better appreciate the relationship between morphology and attenuation coefficient, a color overlay is shown, with neuronal cell bodies in green, and myelin in red. In general layers with more myelin and fewer cell bodies had a higher attenuation coefficient, while layers with more cell bodies had a lower attenuation coefficient.

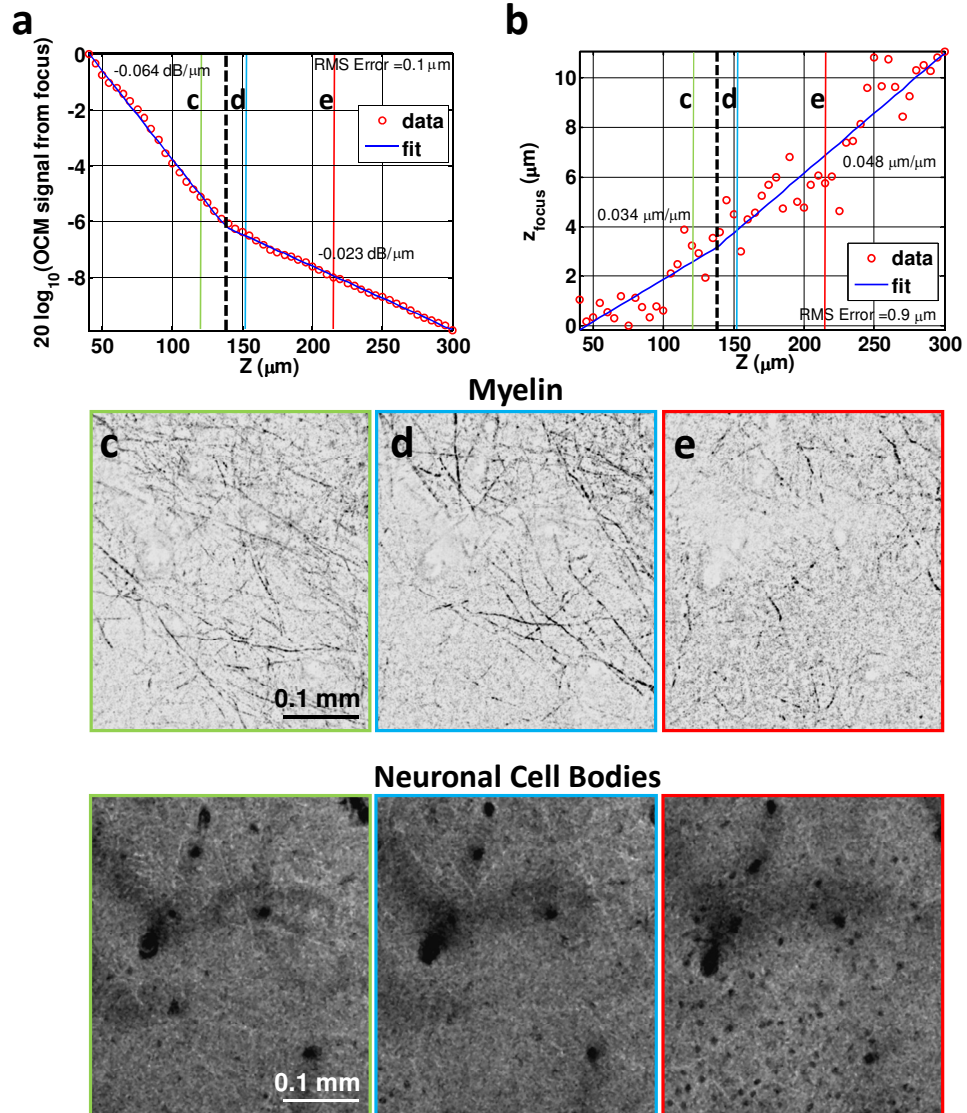


Fig. 9. Changes in optical properties correspond with changes in tissue cellular architecture. (a) OCM signal slope clearly shows a discontinuity (dashed line) at approximately 140 microns, as detected by maximum likelihood fitting, as described in the main text. (b) The refractive index (determined from  $dz_{\text{focus}}/dZ$ ) also shows a discontinuity at 140 microns. (c-e) The images of myelination (above) and cell bodies (below) show a corresponding transition to less myelination and more cell bodies at 140 microns (d), which may explain the discontinuity in optical properties.

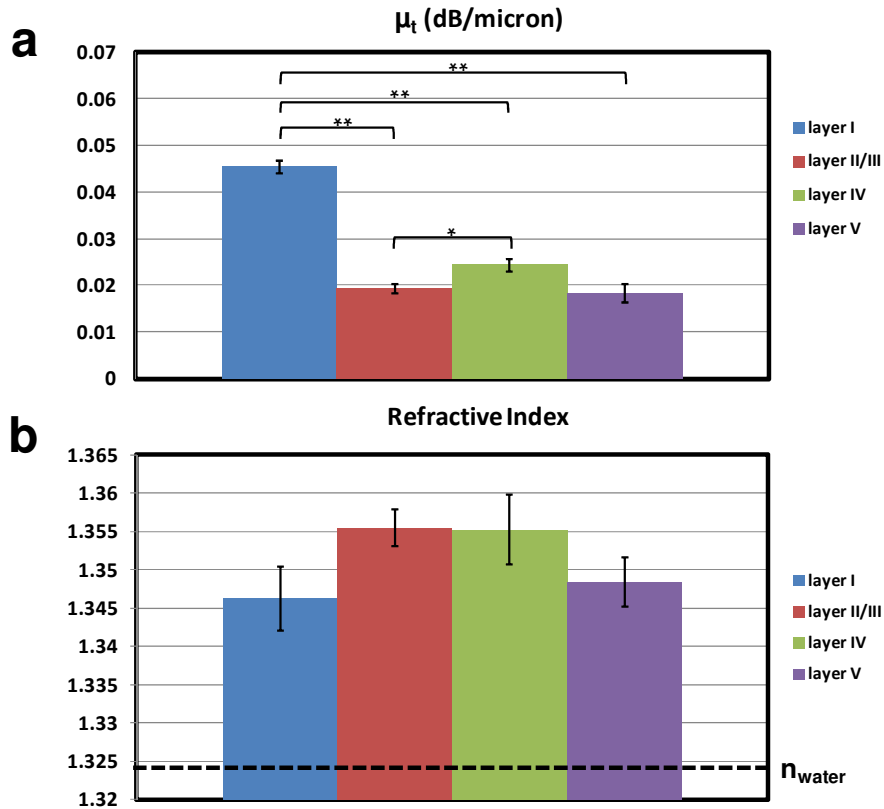


Fig. 10. Attenuation coefficient (a) and refractive index (b), obtained from  $n = 17$  rats. Mean  $\pm$  standard errors for different cortical layers are shown. Layer I had a significantly greater attenuation coefficient than all of the other measured layers, while layer IV had a significantly greater attenuation coefficient than layer II/III, as determined by one-way ANOVA followed by Tukey's honestly significant differences test (\*  $\alpha < 0.05$ , \*\*  $\alpha < 0.01$ ). There were no statistically significant differences between the refractive indices of the different cortical layers. As tissue refractive index is known to exceed the water refractive index by a few percent, the vertical axis in (a) has been shortened in (b) to display only the expected range of tissue refractive indices.

### OCM quantifies optical properties

Quantitative and absolute measurements of the bulk optical properties of brain tissues have twofold significance. Firstly, properties such as the refractive index and scattering of brain tissue may be sensitive indicators of tissue viability. Secondly, as aberrations and scattering are known to limit the penetration depth of optical imaging techniques, measurement of tissue properties is essential for understanding and circumventing depth limitations in *in vivo* microscopy. Dynamically focusing OCM has been previously used to quantitatively determine the refractive index [10,13] and scattering coefficient of tissue [8].

In addition to cellular imaging of cortical layers, we analyzed the refractive index and scattering profiles of brain tissue (Experimental methods) as a function of depth. Scattering is derived from changes in the OCM signal, while the refractive index is derived from changes in the path length to the focus as the objective is translated. (The refractive index and scattering values described here should be interpreted as macroscopic “average” values). As shown in Fig. 8(a) and 8(b), we observed heterogeneous scattering and refractive index profiles in different cortical layers. Maximum likelihood, piecewise linear fitting was performed on the logarithm of the OCM signal arising from the focus (Fig. 8(a)), assuming a priori the presence of 4 boundaries but not their locations. The fitting procedure delineated



five regions of different attenuation coefficients, which corresponded well to layers IA, IB, II/III, IV, and V, as determined based on myelination and cell morphology, shown in Fig. 8(c).

At a depth of approximately 150 microns, the OCM signal slope transitioned abruptly (Fig. 8(a) and Fig. 9(a)). The corresponding sharp transition in attenuation coefficient, from  $\sim 0.045$  dB / micron to  $\sim 0.02$  dB / micron, was present in all animals imaged with OCM (Fig. 10(a)). The depth of this transition corresponded well with the depth at which horizontal myelinated processes disappeared and neuronal cell bodies appeared (Fig. 9(c)–9(e)). We occasionally observed a portion of layer I with few cell bodies and no myelination (layer IB in Fig. 8(c)), which exhibited attenuation coefficients distinctly lower than those of the highly myelinated portion of layer I (layer IA in Fig. 8(c)).

The linear fitting procedure was performed in  $n = 17$  rats. In particular, layer I was found to have a higher attenuation coefficient than the other cortical layers, and layer IV was found to have a higher attenuation coefficient than layer II/III. The results are shown in Fig. 10. As discussed in the Experimental methods, the attenuation coefficient is not unambiguously separable into scattering coefficient and anisotropy [16]; however, under our experimental conditions differences in the attenuation coefficient are predominantly caused by differences in scattering. Thus, as shown in Fig. 10, layers with a high volume fraction of cells (layer II/III) were less scattering than layers with a high volume fraction of neurites (layers I and IV). Myelinated layers were the most scattering. The mean refractive index over all animals and all cortical layers was  $1.352 \pm 0.003$  (s.e.m.). There were no statistically significant differences detected between individual cortical layers, although layers I and V tended to have a lower refractive index than layers II–IV (Fig. 10).

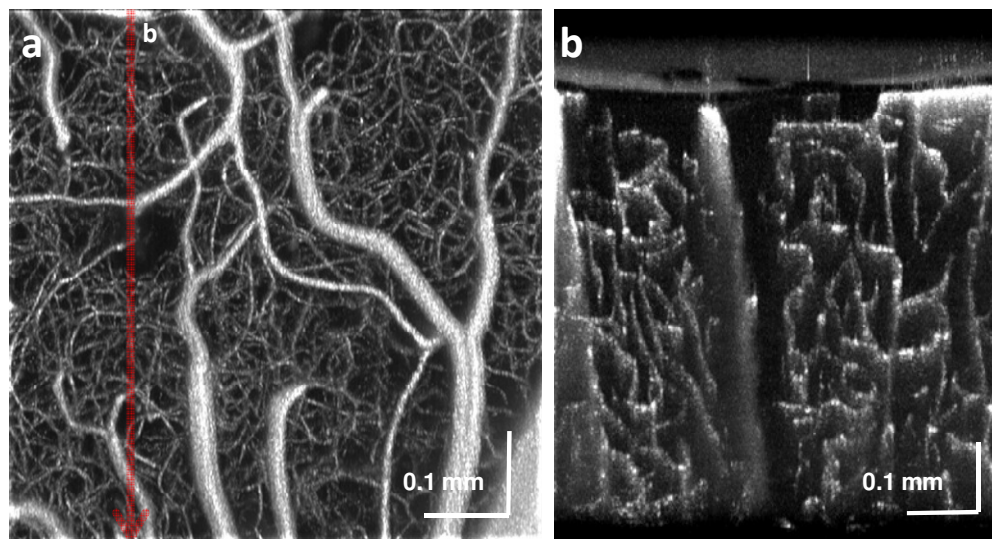


Fig. 11. OCM angiography. OCM angiography visualizes microvasculature using intrinsic contrast (Media 3). (a) Maximum intensity projection image of OCM angiogram from an 80 g Sprague Dawley rat. (b) A maximum intensity projection coronal image of a 50 micron slice is shown, centered at the location of the arrow shown in (a). In particular, the absence of capillaries is notable in the vicinity of the diving arteriole at the center of the coronal image.

### OCM angiography

We adapted our dynamic focusing OCM system to perform angiography. Previously, OCT (Optical Coherence Tomography) angiography techniques have been developed for wide field-of-view imaging [24,25]. These techniques typically suffer from multiple scattering tails beneath vessels; therefore OCT angiograms are typically displayed as *en face* projections and not as depth cross-sections. By comparison, by reducing the depth of focus, our OCM

angiography technique (see Experimental methods) eliminates the multiple scattering tails beneath vessels which are often evident in OCT angiograms. Thus, it is possible to view high quality coronal (depth) cross-sections through the OCM data which show microvasculature with dramatically improved resolution, as shown in Fig. 11(b). In particular, it is possible to discern lower capillary density in the vicinity of the diving arteriole (b), as previously noted by Kasischke et al. using two-photon microscopy [26]. Depth-sectioning of the volumetric angiographic data set is shown in [Media 3](#).

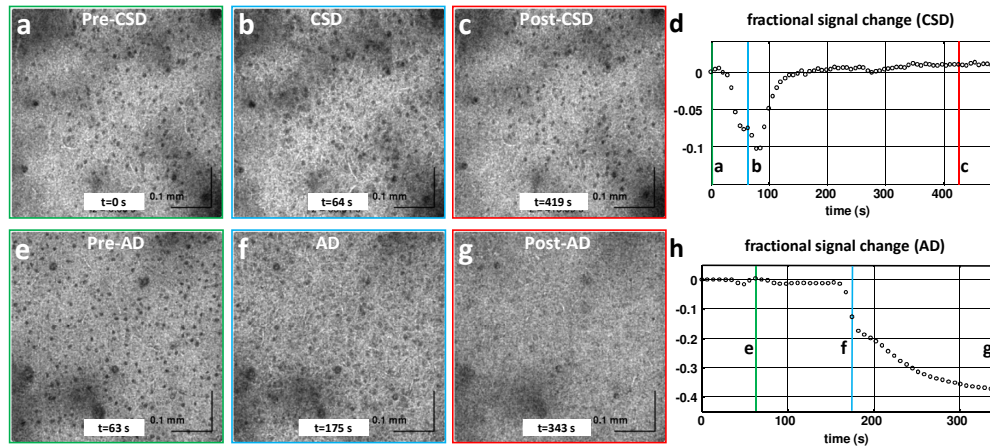


Fig. 12. OCM imaging of cell viability. OCM has the capability to image cell viability *in vivo* based on intrinsic scattering signatures. (a-d) OCM in layer II ([Media 4](#)) shows that depolarization causes transient swelling (b) and increased scattering (d) during cortical spreading depression (CSD). (e-h) OCM in layer II ([Media 5](#)) shows that depolarization causes permanent loss of contrast (g) and increased scattering (h) during anoxic depolarization (AD). These results suggest that OCM may be able to distinguish viable cells from non-viable cells based on intrinsic contrast.

#### OCM images cell viability

We performed OCM imaging during both spreading depression and anoxic depolarization in layer II. Cells swelled (Fig. 12(a)–12(c) and [Media 4](#)) and scattering increased transiently (Fig. 12(d)) during spreading depression. However, cells swelled and lost contrast (Fig. 12(e)–12(g) and [Media 5](#)), while scattering increased permanently during anoxic depolarization (Fig. 12(h)). An increase in scattering results in both an increase in the attenuation coefficient, which reduces the OCM signal and an increase in backscattering, which increases the OCM signal (Experimental methods). Due to the exponential attenuation with depth, at sufficient depths, an increase in scattering reduces the OCM signal. This explains the OCM signal loss during depolarization shown in Fig. 12(d) and Fig. 12(h). The contrast loss and scattering increase accompanying depolarization suggests that OCM can be used to define sensitive intrinsic scattering markers that act as non-invasive indicators of cell status and viability.

#### 4. Discussion

While two-photon microscopy has ushered in a revolution in brain imaging over the past 15 years, several limitations remain. Firstly, penetration depths remain limited to a few hundred microns, and typically, either exogenous dyes or transgenic animals are required. Here we present a different strategy for deep tissue brain imaging using intrinsic scattering contrast, i.e. contrast arising from endogenous properties of biological tissues. We demonstrate imaging depths of 2.5-3x higher than standard two-photon microscopy in the living brain. This penetration depth was achieved with a continuous wave infrared superluminescent diode light source, with optical powers at the sample of approximately 4 mW.

Our data show that OCM enables visualization of cell bodies through a negative contrast mechanism. Neurites (axons, dendrites) exhibit high backscatter due to their size (on the order of a wavelength) and refractive index contrast [27]. Even so, due to the high refractive index of myelin, myelinated axons in the *en face* plane appear as highly scattering processes against an already highly scattering background, and can thus be enhanced through performing a maximum intensity projection.

By comparison, neuronal cell bodies appear as low scattering regions. However, the cell body is known to consist of multiple organelles of higher refractive index than the cytosol. Therefore, one possible explanation for the relatively low scattering from neuronal cell bodies is that the organelles and subcellular structures are packed tightly enough to present negligible refractive index variations on a sufficiently large spatial scale that would lead to significant backscatter. An alternative explanation is that the large-scale refractive index variations between cytosol and organelles within a cell are much smaller than refractive index variations between neurites and extracellular fluid. Therefore, in viable tissue, intracellular organelles in the cell body are tightly packed or refractive index variations are not significant; therefore backscattering from organelles is low compared to backscattering from neurites. In models of light scattering designed to detect pre-cancerous changes, cell nuclei were assumed to account for the periodic fine structure in reflectance from biological tissue [28]. However, recent experimental measurements of refractive index have shown relatively small variations in refractive index within the cell itself and in particular, less refractive index contrast between the nucleus and other cellular regions than was previously thought [29]. This recent work is in agreement with our observation that neuronal cell bodies appeared as relatively lower scattering regions against a highly scattering background of neurites. A similar phenomenon occurs in the retina, where OCT images show highly backscattering plexiform layers and less backscattering nuclear layers [30].

Our data show that anoxic depolarization is accompanied by cell swelling and increased scattering from subcellular compartments, resulting in a loss of contrast. A number of physiological processes occur upon energy failure. Firstly, channels open and the cell swells as water invades the intracellular space. At first glance, entrance of the water into the intracellular space would seem to lead to a reduction in backscatter as cell size increases [31–33] and the average cellular refractive index is reduced. However, the entrance of water into the cell may also reduce the organelle packing density and increase inhomogeneities in the intracellular refractive index, thereby leading to wavelength-scale intracellular refractive index variations that result in high scattering. Intracellular organelle swelling [34] and shape changes, as well as membrane failure, nuclear condensation and fragmentation may also lead to increased scattering. The neurite environment also increases scattering after anoxic depolarization due to processes such as dendritic beading [35,36]. Diffusion weighted MRI [37–39] measures changes in the apparent diffusion coefficient are caused by intercompartmental water shifts associated with cytotoxic edema. Our results suggest that analogous optical scattering markers can be defined to measure cell viability using intrinsic contrast.

We anticipate that these results will enable a number of novel *in vivo* and *ex vivo* optical imaging paradigms. Volumetric OCM data may provide information about cell density, volume, myelination, and capillary density at cortical depths exceeding 1 mm. These *in vivo* techniques have potential advantages over conventional histological methods, since measurements can be performed repeatedly without animal sacrifice, and do not require fixation, slicing, or staining. The capability to image myelinated axons using only intensity-based information, as opposed to birefringence [40], will enable all-optical tractography and studies of brain connectivity. As myelin presents the main barrier that causes anisotropic diffusion in white matter, our measurements of microscopic fiber directionality could be used to directly validate diffusion MRI [41–43]. While current imaging depths are already sufficient to image the entire cortex in mice, alternative imaging geometries may enable greater depth penetration, and improve sensitivity to non-transverse fiber orientations. Further

studies will be required to investigate changes in scattering contrast after fixation, dehydration, and optical clearing procedures.

## **5. Conclusion**

In conclusion, we demonstrate imaging of highly scattering cortical tissue *in vivo* at the cellular level with intrinsic contrast. Through the use of OCM with dynamic focusing and image processing techniques, we demonstrate imaging of myelination and neuronal cell bodies, index of refraction and scattering measurements, angiography, and imaging of intrinsic markers of cell viability. The concept of cellular imaging with intrinsic contrast has potential applications in longitudinal studies of development, disease progression and treatment response.

## **Acknowledgments**

We acknowledge helpful suggestions or references from James Fujimoto, Bruce Rosen, Jeff Lichtman, Cenk Ayata, Eng Lo, Jean Augustinack, David Boas, Anna Devor, Sava Sakadzic, Mohammed Abbas Yaseen, and Maria Angela Franceschini. We thank Maria Angela Franceschini for permission to use the OCT microscope. We thank Weicheng Wu for the rat surgery. We acknowledge support from the National Institutes of Health (K99NS067050, EB001954 R01), the American Heart Association (11IRG5440002), and the Glaucoma Research Foundation Catalyst for a Cure 2.